# TOMOGRAPHY OF MOVING TARGETS (TMT) FOR SECURITY AND SURVEILLANCE

Michael C. Wicks, Braham Himed
*Air Force Research Laboratory Sensors Directorate*
*26 Electronic Parkway Rome, NY 13441*

Harry Bascom, John Clancy
*L3-Communications Analytics Corporation*
*Advanced Technologies & Law Enforcement Sector*
*1300 B Floyd Avenue Rome, NY 13440*

**Abstract**

In order to improve upon automated sensor performance for security applications in public and private settings, numerous alternative sensor designs have been developed to provide affordable and effective detection and identification performance. Radio frequency (RF) sensors offer a balanced approach to system design for a wide variety of geometries and threat targets. These threat targets include persons carrying weapons and explosives, portable containers with contraband including cargo boxes, suitcases, and briefcases and fixed structures including building or underground facilities harboring criminals, terrorist or enemy combatants. In order to achieve the resolution required for the detection and identification of threat targets, separation of interference from the target response is essential. High bandwidth offers a conventional approach to high resolution sensing of the threat. An alternative approach, one based upon wide angular bandwidth (spatial diversity), is presented here.

This chapter addresses the issue of spatial diversity in radar applications. There has been an increased need for information via radio frequency (RF) detection of airborne and ground targets while at the same time the electromagnetic spectrum available for commercial and military applications has been eroding. Typically, information concerning ground and air targets is obtained via monostatic radar. Increased information is often equated with increased bandwidth in these monostatic radar systems. However, geometric diversity obtained through multistatic radar operation also affords the user the opportunity to obtain additional information concerning these targets. With the appropriate

signal processing, this translates directly into increased probability of detection and reduced probability of false alarm. In the extreme case, only discrete Ultra Narrow Band (UNB) frequencies of operation may be available for both commercial and military applications. As such, the need for geometric diversity becomes imperative.

**Keywords:**

tomography; moving targets; spatial diversity; ultra narrow band (UNB); monostatic radar; multistatic radar.

## 1. Inroduction

The electromagnetic spectrum available for commercial and military applications is continuously being eroded while the need for increased information via RF detection of threat targets is increasing. Typically, military information concerning ground and air targets is obtained via monostatic radar. Increased information is often equated with increased bandwidth in these monostatic radar systems. However, geometric diversity obtained through multistatic radar operation also affords the user the opportunity to obtain additional information concerning these targets. With the appropriate signal processing, this translates directly into increased probability of detection and reduced probability of false alarm. In the extreme case, only discrete Ultra Narrow Band (UNB) frequencies of operation may be available for both commercial and military applications. As such, the need for geometric diversity becomes imperative. In addition, geometric diversity improves target position accuracy and image resolution which would otherwise remain unavailable with monostatic UNB radar.

However, coherent signal processing of a multitude of UNB radar signals emanating from and received by geometrically diverse sites requires more than the simple processing (multiplication and addition) which forms the basis for synthetic aperture radar (SAR) or even moving target indication (MTI). Classical tomographic signal processing offers one basic (albeit sub-optimum) approach to the processing of multi-frequency UNB radar data collected via geometrically diverse transmit and receive sites. Tomography is applicable to radar even though the basic mechanism for re-radiation is the back scatter and forward scatter of electromagnetic waves by moving objects, and not reflection and transmission as in tomography. When modest increases in bandwidth are permitted at each transmitter site, further complications arise in the coherent signal processing required for target detection and interference suppression. While classical tomography (designed to operate under the monochromatic assumption) is applicable as a baseline, this mathematical formulation has been modified and extended to optimize target

detection and interference rejection in the Tomography of Moving Targets. It is the objective of this chapter to present a practical approach to target detection and interference rejection via tomographic processing of geometrically diverse, multi-frequency, multistatic, UNB radar data. The emphasis in this chapter is on the detection of slower moving weak target returns.

In classical radar, frequency diversity offers one method to obtain additional information about threat targets. With the most basic form of frequency diversity, namely increased bandwidth, high range resolution is afforded to the user. With high range resolution comes increased target-to-clutter ratio (assuming the target is not over-resolved), while target-to-noise is unavoidably reduced since increased bandwidth results in additional unwanted thermal noise competing with and potentially masking weak target returns. Geometric diversity also offers the potential for increased resolution, and is a dual to frequency diversity (increased bandwidth) in classical monostatic radar. In the extreme case, $360^o$ of geometric diversity (across a large number of sensor sites) offers sub-wavelength resolution, even under the monochromatic assumption. Operating with UNB radar signals permits a substantial reduction in thermal noise power as well, improving overall detection performance. Here, sophisticated tomographic signal processing is required to extract a moving target from clutter. In this chapter, the Tomography of Moving Targets is developed and demonstrated for geometrically diverse, multi-frequency, multistatic, UNB radar. Additionally, only moderately directive broad beam antennas (approximately $60^o$) are used to radiate and receive UNB signals for the Tomography of Moving Targets, unless otherwise justified by analysis.

A baseline design and approach has been developed to demonstrate the Tomography of Moving Targets. Preliminary simulations and analysis have been performed indicating how well this approach addresses the stated goals of increased target detection/identification and improved target location via the analysis of geometrically diverse, multi-frequency, multistatic UNB radar data. The number and locations of transmitter and receiver sites, and the UNB frequencies are selected heuristically.

## 2. Tomography Concept and Framework

The TMT concept leverages the spatial or geometric diversity of a multistatic ground based 'netted' radar to deliver high resolution MTI. The TMT concept provides the resolution of conventional wideband MTI radars, while using UNB signals. These UNB signals are particularly attractive with consideration to the ongoing spectral erosion due to the

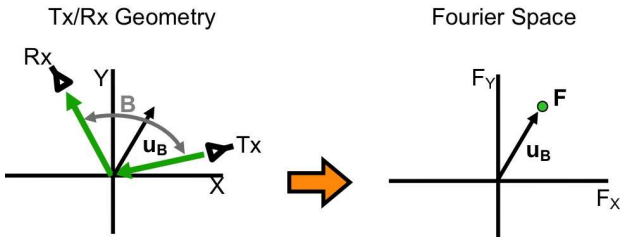


*Figure 1.* Sensor Geometry and Fourier Space Relationship

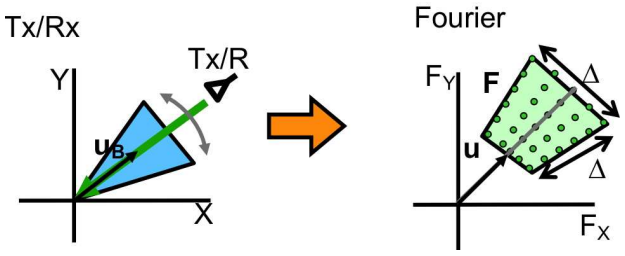


*Figure 2.* Fourier Space Sampling and Scene Resolution

wireless escalation. The TMT effort is considering both ground and airborne MTI applications. Some sites have collocated transmitters and receivers, while other sites are receive only. By locating the sites in a somewhat random manner, the geometric diversity is enhanced.

The radar data samples are mapped onto a polar grid in the spatial Fourier domain. The positions of the transmitter and receiver along with the signal's instantaneous frequency determines the Fourier space sample position, as given by equation 1. This relation is illustrated in figure 1. A bistatic sensor configuration is shown with a bistatic angle (B), $\mathbf{u}_B$ is the bistatic bisector. This geometry and signal frequency maps into the Fourier space sample given by the vector $\mathbf{F}$. As shown, the sample position lies along the bistatic bisector with a magnitude proportional to the instantaneous frequency scaled by $\cos B/2$.

$$\mathbf{F} = \frac{4\pi f}{c} \cos \frac{B}{2} \mathbf{u}_B \tag{1}$$

where $f$ is the frequency, $c$ is the speed of light, $B$ is the bistatic angle, and $\mathbf{u}_B$ is the bistatic bisector unit vector.

Figure 2 illustrates a typical Fourier space sampling as provided by a monostatic SAR. As shown, the samples in the radial dimension straddle a term proportional to the carrier frequency and have an extent proportional to the signal bandwidth. Samples in the angular dimen-

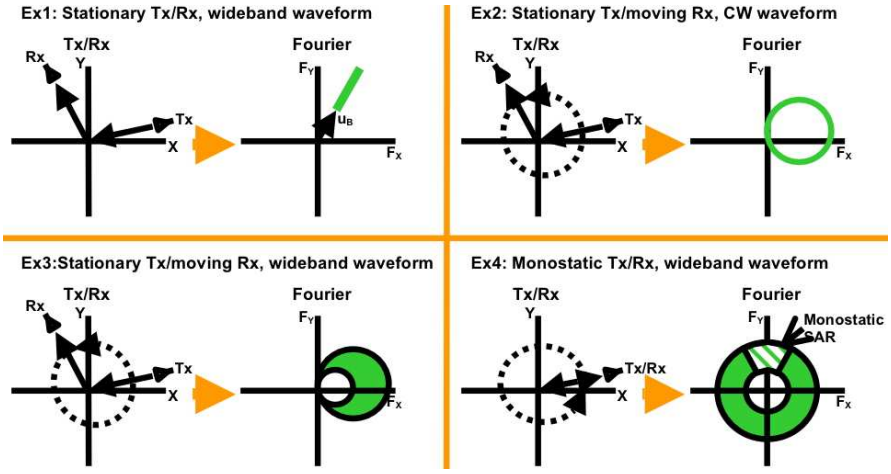


*Figure 3.* Sensor Geometry and Fourier Space Relationship Examples

sion correspond to pulse numbers of the coherent processing interval. In the monostatic case, the angular extent of the samples is the same as the angular aperture created by the synthetic aperture.

Recall that the image resolution, $\delta_{\text{DOWN}}$ and $\delta_{\text{CROSS}}$, is inversely proportional to the size of the region of Fourier space sampled, as given by 2, where $\Delta u$ and $\Delta v$ are the sizes of the sides of the sampled region. The unambiguous scene size is inversely proportional to the Fourier space sampling frequency.

$$\delta_{\text{DOWN}} = \frac{2\pi}{\Delta u}; \quad \delta_{\text{CROSS}} = \frac{2\pi}{\Delta v} \quad . \tag{2}$$

In the spatial Fourier domain, radial band limiting is due to the finite bandwidth of the transmitted pulse while angular band limiting is due to the finite diversity of look angles. With variations of frequency and angular diversity, the spatial Fourier domain can be sampled in a variety of ways. This spatial Fourier domain sampling impacts the resulting image's resolution. Higher resolution is achieved with greater diversity, be it frequency, angular or some combination of both. Image resolution is inversely proportional to the size of the region of Fourier space sampled. Figure 3 illustrates, by way of four examples, how different bistatic geometries and waveforms map into Fourier space.

In example 1, a fixed bistatic geometry and a wideband waveform result in Fourier space sampling along a radial line, at the bistatic bisector. In example 2, a fixed frequency (CW) waveform is used as the receiver is moved in a circle about the origin. The resulting Fourier space sam-

pling is a circle who's center is offset from the origin. In example 3, a wideband waveform is used as the receiver is moved in a circle about the origin. The resulting Fourier space sampling is a combination of the results of examples 1 and 2. For completeness, example 4 shows the case of a wideband waveform and a monostatic geometry. The resulting Fourier space sampling has a donut shape. The typical monostatic SAR doesn't fly a circular flight path around a scene, but instead flies a straight line path, the resulting Fourier space sampling is highlighted as a wedge of the donut.

SAR and tomography may be viewed in terms of image reconstruction from a bandlimited region in 2-D Fourier space. Resolution, for both SAR and tomography, is a function of the bandwidth available in the 2-D Fourier space. The conventional SAR resolution formulas are approximations to this, for the limited cases of small apertures and percent bandwidths. Narrowband, wide angle tomographic imaging achieves the resolution of wideband, narrow angle SAR systems by trading frequency for spatial diversity. The resolution limit for this system is about one third of a wavelength. A comparison of Fourier space sampling provided by mono, bi and multi-static SAR and their corresponding resolution is illustrated in figure 4. The colored area represents the region of Fourier space sampled. The simplified resolution formulas for small aperture and percent bandwidth are given for the mono and bistatic cases. For the bistatic case, assume a pseudo-monostatic geometry with the transmitter in a fixed position and the receiver forming the same aperture as in the monostatic case. The angular sampling is compressed in the bistatic case, compared to the monostatic case, due to sampling occurring on the bistatic bisector. This results in loss in cross range resolution. In the multistatic case, a circular region could potentially be sampled. The radius of this circle is proportional to the highest frequency used and the resulting image has a resolution of a third of a wavelength of this frequency.

It is interesting to note that the resolution result for the monostatic SAR case can be derived using the tomography/Fourier space or the radar range/Doppler principles. However, the resolution result for the multistatic SAR is easily understood using the tomography/Fourier space principles. To compare the resolution capabilities of these sensor configurations, consider an UWB monostatic SAR with a 50% bandwidth. It has a range resolution of $\lambda$ and a pixel area of $\lambda^2$. Multistatic SAR with a range resolution of $\frac{\lambda}{3}$ has a pixel area of $\frac{\lambda}{9}$, yielding a 9.5 dB improvement over monostatic.

Consider a geometry where multiple transmitters and receivers are positioned on circle, surrounding the region to be imaged. Each trans-

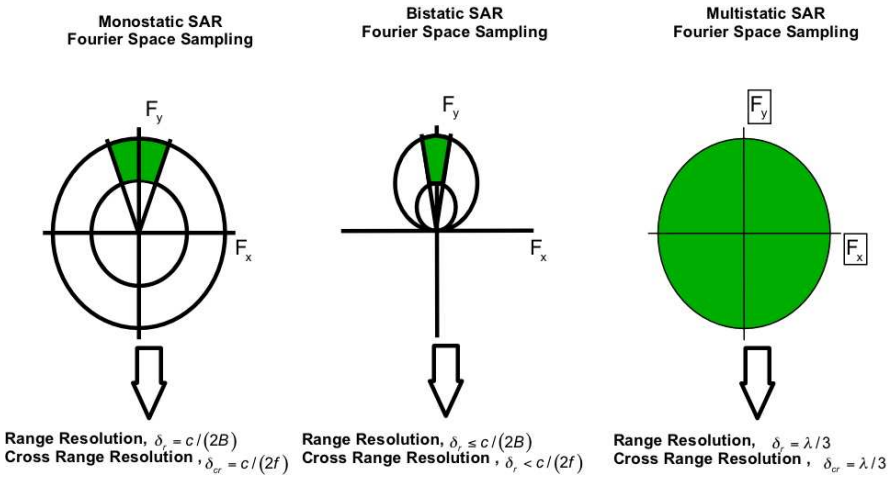


*Figure 4.* Comparison of Fourier Space Sampling

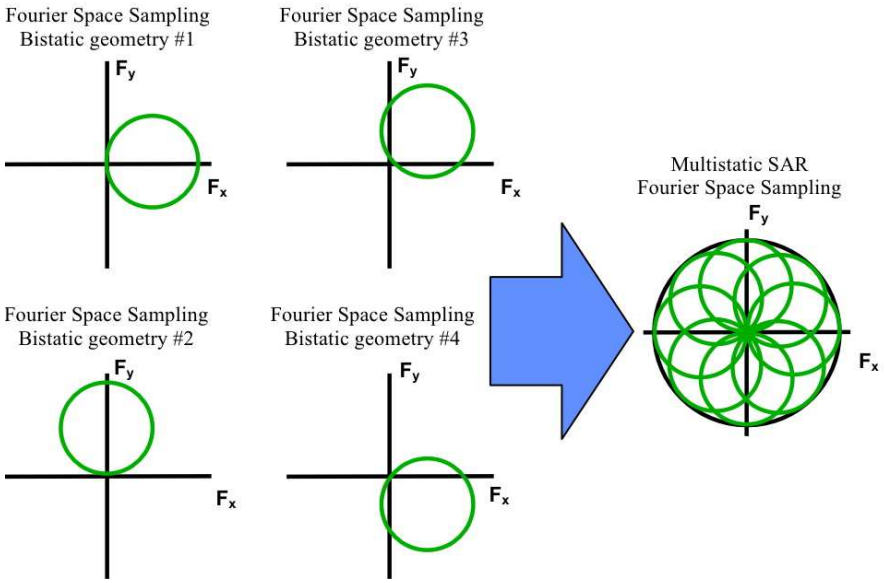


*Figure 5.* Multistatic Fourier Space Sampling

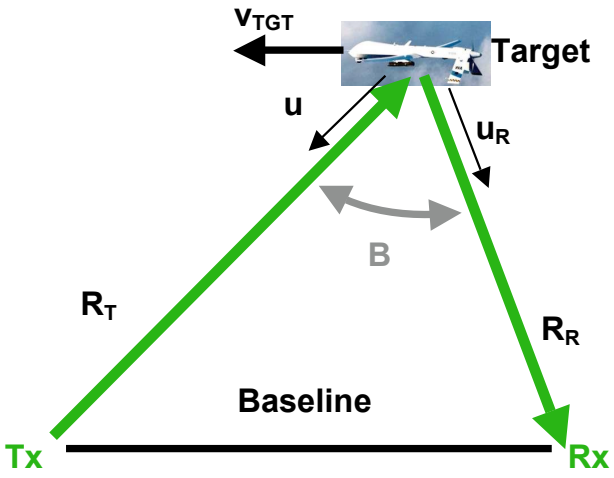


*Figure 6.* Bistatic Geometry

mitter with all receivers creates a multistatic geometry with Fourier space sampling as shown in figure 5. In this approach, it is assumed that the transmitted signal is narrowband. By piecing together the regions sampled by each multistatic transmitter/receiver combination, the result is a multistatic Fourier space sampling.

## 3. Bistatic Geometry and Observables

The bistatic geometry discussed in this section is shown in figure 6. The round trip path causes the received target return to be time delayed ($t_d$) from the transmitted signal, given by equation 3, where $R_T$ and $R_R$ are the distances from the target to the transmitter and receiver. For the case of stationary, ground based, transmitter and receiver, the Doppler frequency ($f_D$) of a target return is due to the motion of the target. The target Doppler is computed as the sum of the target's velocity vector ($v_{TGT}$) dot product with unit vectors pointing from the target to the transmitter ($u_T$) and receiver ($u_R$) as given by equation 4.

$$\mathbf{t}_d = \frac{\mathbf{R}_T + \mathbf{R}_R}{\mathbf{c}}, \tag{3}$$

$$\mathbf{f}_D = \frac{\mathbf{v}_{\text{radial}}}{\lambda} = \frac{(\mathbf{v}_{\text{TGT}} \cdot \mathbf{u}_T + \mathbf{v}_{\text{TGT}} \cdot \mathbf{u}_R) \cdot f}{\mathbf{c}}. \tag{4}$$

Previously, tomography applied to radar has been limited to only SAR applications. In this chapter, the tomographic paradigm is extended to MTI. When considering multistatic geometries and moving targets, the

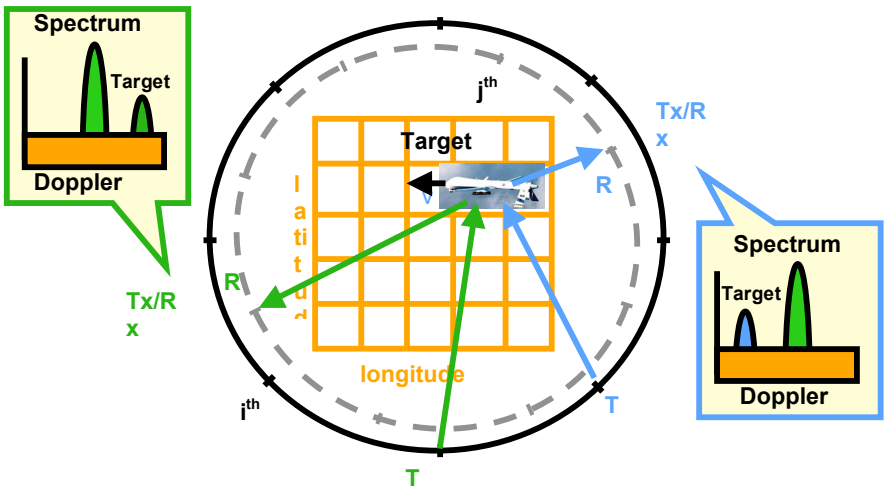


*Figure 7.* Multistatic MTI — Target Doppler Issue

issue arises of a target having a different Doppler for each of the transmit/receive pairs, as illustrated by figure 7. Conventional processing, employing FFTs for spectral analysis, results in an overwhelming confusion factor. In response to this issue, a matched filter processing (MFP) algorithm is developed.

## 4. Matched Filter Processing (MFP)

MFP has its origin in SAR image reconstruction and is considered a spatial domain image reconstruction technique. It implements a 'matched filter' for each pixel of a scene. This matched filter simply attempts to replicate the signal's expected delay and Doppler, which can be viewed as a 'steering' vector. The matched filter and received signal is tested for correlation. The extension to moving targets involves much more work. For each scene pixel, matched filters are built for a range of hypothesized target velocities (speeds and headings). In adaptive processing, a Doppler steering vector is used. In MFP, the Doppler steering vector is generalized to a velocity steering vector. Assume the transmitted signal ($\mathbf{T}$) to be a CW tone, as given by equation 5, where f is the carrier frequency and $\mathbf{t}$ is a time vector of a coherent processing interval (CPI) at a sample rate required by the expected IF bandwidth. The receive signal ($\mathbf{R}$) is the superposition of time delayed and Doppler shifted target signals plus noise ($\mathbf{N}$) (equation 6). Each target has a velocity vector (speed and heading) that provides a unique Doppler for

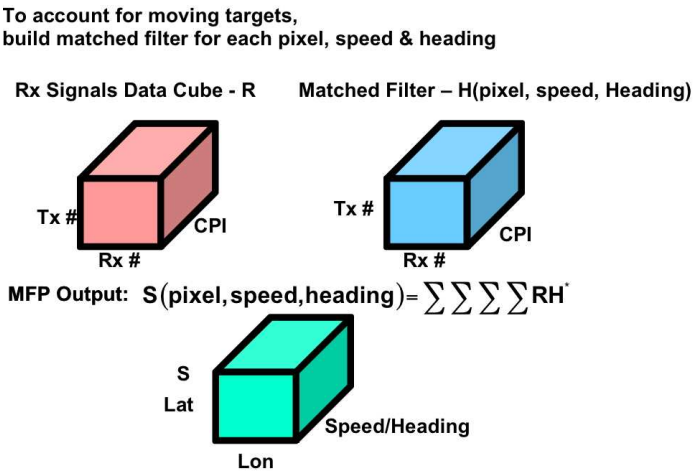


*Figure 8.* MFP Formulation

each transmit/receive pair. Likewise the target's time delay also varies for each transmit/receive pair.

$$\mathbf{T}_i\left(f\right) = e^{j2\pi\cdot f\cdot \mathbf{t}}, \tag{5}$$

$$\mathbf{R}_{il}\left(\mathbf{f}\right) = \sum_{k=1}^{K} e^{j2\pi\cdot\left(f+f_{D_{ilk}}\right)\cdot\left(\mathbf{t}-t_{d_{ilk}}\right)} + \mathbf{N}, \tag{6}$$

where $i$ is the Tx index (location), $l$ is the Rx index (location), $k$ is the Target index, $\mathbf{t}$ is the time sample vector for CPI, and $\mathbf{N}$ is the additive noise.

For MFP, a matched filter ($\mathbf{H}$) is computed for each scene pixel, as a time delay, and hypothesized target velocity, as given by equation 7. To cover all pixels and target velocities, a bank of filters are employed, using the velocity steering vector. The MFP output ($\mathbf{S}$) is computed as a conjugate inner product of the received signals and matched filter over all transmit/receiver pairs, frequency and time, as given by equation 8.

$$\mathbf{H}_{il}\left(f, pixel, \mathbf{v}_{TGT}\right) = e^{j2\pi\cdot\left(f+f_{D_{il}}\right)\cdot\left(\mathbf{t}-t_{d_{il}}\right)} \tag{7}$$

$$\mathbf{S}\left(pixel, \mathbf{v}_{TGT}\right) = \sum_{i}\sum_{l}\sum_{f}\sum_{t} \mathbf{R}_{il}\left(f\right)\cdot\mathbf{H}^{*}_{il}\left(f, pixel, \mathbf{v}_{TGT}\right) \tag{8}$$

The MFP process is illustrated in figure 8. The received signal, for all transmit/receive pairs, over a CPI forms a data cube. The matched

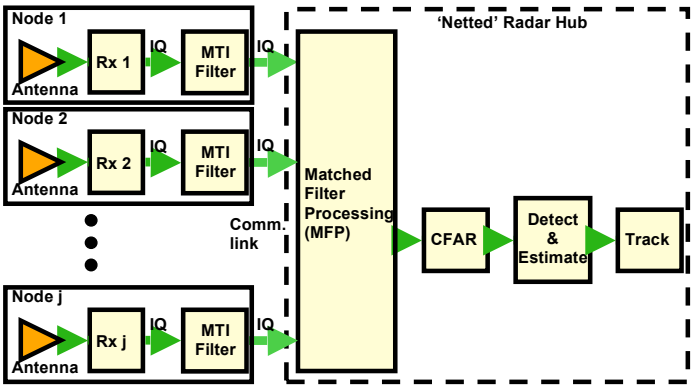


*Figure 9.* System Receive Processing Block Diagram

filter, for a particular scene pixel and target velocity, also forms a data cube. For multiple operating frequencies, additional cubes would be formed. A single MFP output, a pixel and velocity, is the inner product of these cubes. The process is repeated for all pixels and hypothesized target velocities. Target detection is then performed on the **S** cube.

## 5. TMT Netted Radar System

The 'netted' radar receiver system block diagram is shown in figure 9. The various receiver positions or sites are designated as nodes. These receivers may employ multiple channels covering multiple bands. The in-phase and quadrature (IQ) data is MTI filtered to pass moving targets and filter out stationary ground clutter. The IQ data from each node is communicated to a central processing location, referred to as the netted radar 'hub'. The MFP is commenced by assembling the received signal data cube and matched filtering it. The MFP output is then sent to a CFAR detector, followed by detection and tracking stages.

## 6. TMT MFP Simulation

A simulation of the TMT process is being used to probe the various issues and projected performance. Consider the following parameters:

- Sensors, Targets are all in a plane (flat earth, no altitude)
  - 10 Transmitters
  - 30 Receivers
  - 5 Targets
  - Area Of Interest (AOI) = 1km × 1km (25 m pixel spacing)

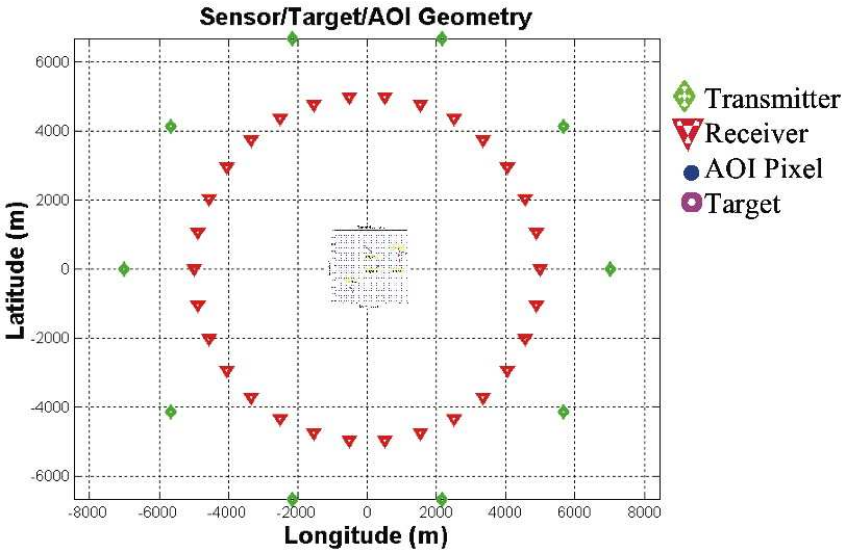


*Figure 10.* Test Geometry

- Waveform
  - 4 CW Tones
  - Frequencies = 1, 2, 3 & 4 MHz
  - CPI = 5 sec

The sensor geometry is shown in figure 10. The 10 transmitters and 30 receivers form concentric circles about the scene to be imaged. This geometry was used out of convenience and to be familiar to the typical tomographic geometry. The actual geometry may be more random and is accommodated by MFP. A small scene of 1km by 1km was used for computational reasons. Five targets were positioned within the scene. Each target has a unique velocity vector.

The Fourier space sampling, corresponding to the sensor geometries and frequencies used, is shown in figure 11. The left side shows the sampling for one transmitter and all receivers, while the right side shows the entire sampling. Based on this sampling, the expected spatial resolution is about 25 meters.

A zoom-in view of the scene, figure 12, shows the area of interest (AOI) pixel locations and target locations. The targets were spaced so that they should be spatially resolved, based on the expected 25 meter resolution.

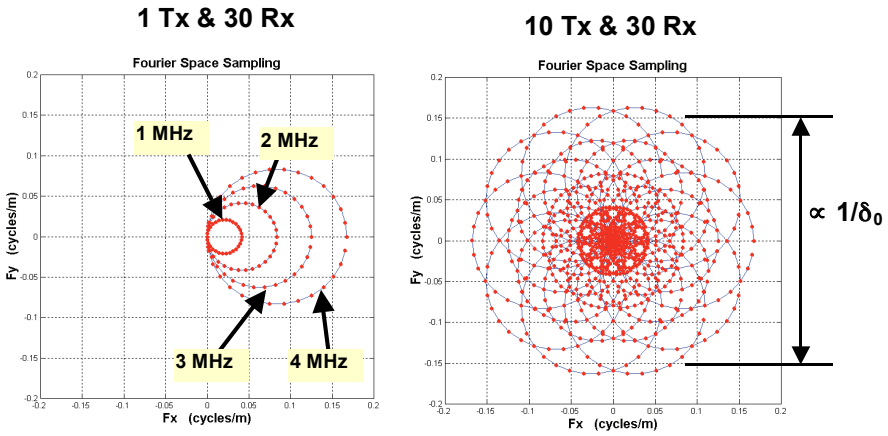


*Figure 11.* Fourier Space Sampling and Expected Resolution

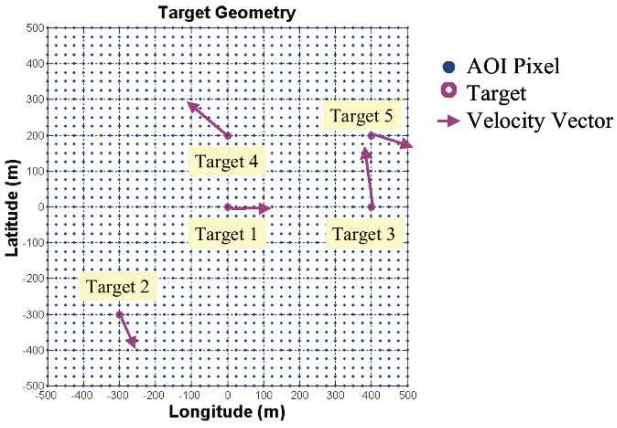


*Figure 12.* Scene Geometry — Zoom In

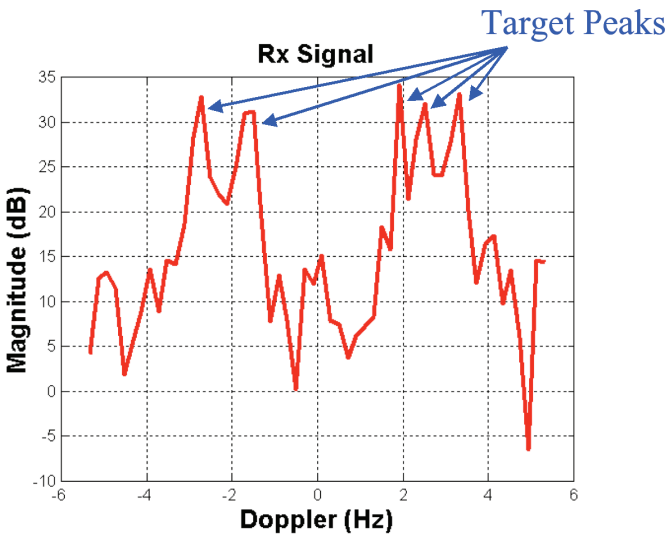


*Figure 13.* Received Signal Spectrum — Single Tx/Rx Pair

The received signal spectrum for a single transmit/receive pair is shown in figure 13. For this pair the five target responses are clearly visible. The noise floor is approximately 10 dB, providing a signal to noise ratio (SNR) of at least 20 dB. Note that ground clutter was not modeled and is assumed to be removed by employing the MTI filter.

The MFP results are shown in figure 14. The output cube **S** is in the upper left. Slices of latitude and longitude, for a particular velocity (speed/heading), are shown. These slices show the likely target detections that a 3-D CFAR process would find. The targets clearly stand out from the background. The targets are also resolved spatially, demonstrating that geometrically diverse UNB systems can provide high spatial resolution.

The MFP output SNR was good ($> 15$ dB) for 4 of 5 targets. The table in figure 15 shows the target truth table and the MFP estimates. The target location estimates were quite encouraging. The estimated velocities were moderately acceptable, this aspect will require further analysis to find the appropriate spatial and frequency diversity to improve the velocity estimate.

## 7. Detection Perfomance

The probability of detection (Pd) performance versus SNR, of a non-fluctuating target with a probability of false alarm ($P_{FA}$) of $10^{-6}$, for a

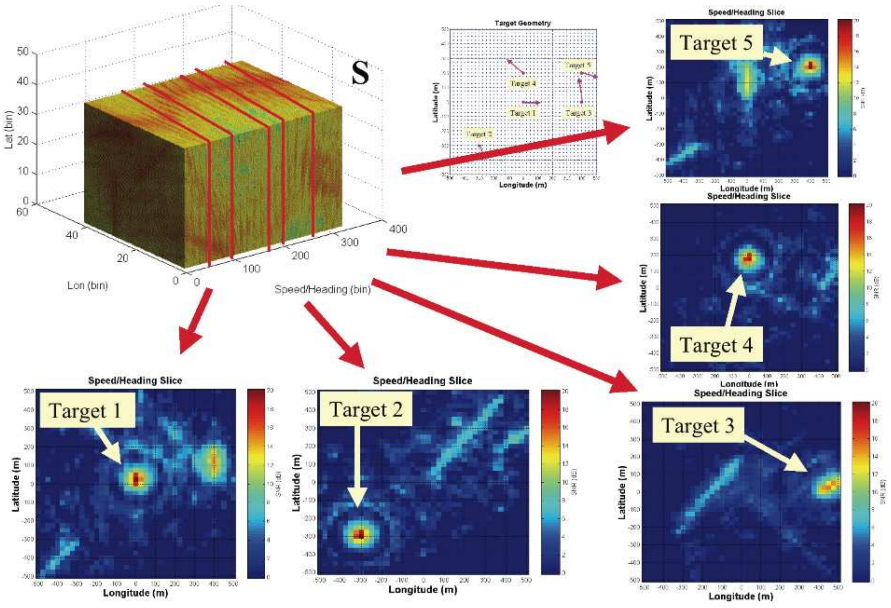


*Figure 14.* MFP Output Cube and Velocity Slices

| Target # | Target Truth Position and Velocity | | | | | Target Estimates Position and Velocity | | | | |
|---|---|---|---|---|---|---|---|---|---|---|
| | Lon (m) | Lat (m) | Alt (m) | Speed (m/s) | Head (°T) | Lon (m) | Lat (m) | Alt (m) | Speed (m/s) | Head (°T) |
| 1 | 0 | 0 | 0 | 124 | 89.1 | 0 | 25 | 0 | 123 | 282 |
| 2 | -300 | -300 | 0 | 104 | 156.9 | -300 | -300 | 0 | 146 | 47 |
| 3 | 400 | 0 | 0 | 193 | 351.9 | 450 | 25 | 0 | 200 | 313 |
| 4 | 0 | 200 | 0 | 151 | 309.6 | 0 | 175 | 0 | 192 | 172 |
| 5 | 400 | 200 | 0 | 130 | 108.2 | 400 | 200 | 0 | 131 | 156 |

*Figure 15.* Target Detections

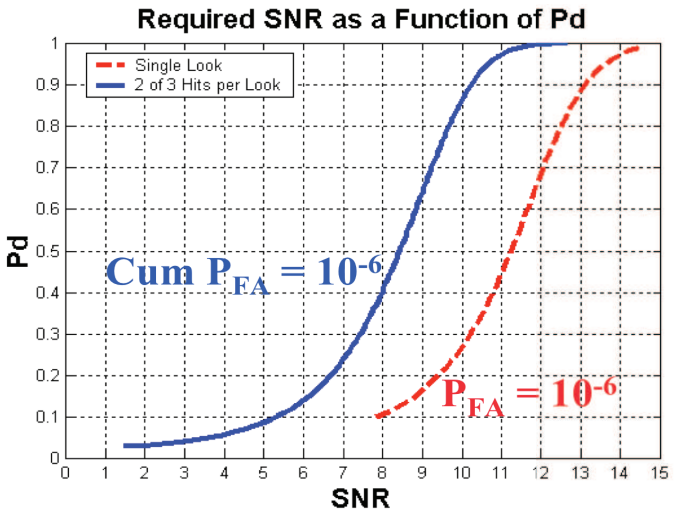


*Figure 16.* Detection Performance

single look or CPI is shown by the red (dashed) curve in figure 16. For an SNR of 12 dB, the single look Pd is 0.7. The cumulative Pd for an M hits of N looks scheme, with M=2 and N=3 and a cumulative $P_{FA}$ of $10^{-6}$, is shown by the blue (solid) curve. This shows that the same 12 dB SNR provides a cumulative Pd of 0.99. The TMT detection processing will likely employ such schemes to improve detection performance.

## 8. Summary

The TMT concept shows promise for providing high resolution surveillance of ground and airborne moving targets with geometrically diverse UNB transmissions. The UNB signals provide relief when faced with the consequence of ongoing spectrum erosion. The simulation activities have begun to probe fundamental issues of imaging quality and required diversity in frequency and space. Future work will bring more reality into consideration. Issues such as clutter and MTI filters, target cross section fluctuations, and netted radar architectures will be explored.

## 9. Acknowledgements

The authors would like to acknowledge the management of the Air Force Research Laboratory, Sensors Directorate, for supporting this research.

## References

[1] H. Bascom, J. Clancy. HF Imaging Techniques for Ground Penetration, Phase II Final Report, Decision-Science Applications, Inc., Report No. 147/1762, Aug 1998.

[2] H. Bascom, J. Clancy. Ogrodnik HF/VHF Bistatic SAR for Buried Target Detection Experimental Results. *44th Annual Tri-Service Radar Symposium* , June 1998.

[3] H. Bascom, J. Clancy. Ogrodnik Bistatic Approaches to Below Ground Target Imaging, *43rd Annual Tri-Service Radar Symposium Record*, June 1997.

[4] R. McMillan, et al. Bistatic Surveillance of Surface Targets - Concept Analysis, *42th Annual Tri-Service Radar Symposium Record*, June 1996.

[5] C. Jakowatz, D. Wahl, P. Eichel, D. Ghiglia, P. Thompson. *Spotlight-Mode Synthetic Aperture Radar: A Signal Processing Approach*, Kluwer Academic Publishers, 1996.

[6] H. Li, F. Lin, Y. Shen, N. Farhat. A Generalized Interpretation and Prediction in Microwave Imaging Involving Frequency and Angular Diversity, *Journal of Electromagnetic Waves and Applications*, vol. 4, no. 5, pp. 415–430, 1990.

[7] N. Willis. *Bistatic Radar*, Artech House, 1991.

[8] D. Mensa. *High Resolution Radar Cross-Section Imaging*, Artech House, 1991.